Journal of Materials Chemistry C

ROYAL SOCIETY OF CHEMISTRY

PAPER

View Article Online
View Journal | View Issue

Cite this: J. Mater. Chem. C, 2022, 10, 15897

The impact of Yb^{3+} concentration on multiband upconversion in a single $NaYF_4$:Yb/Er microcrystal determined *via* nanosecond time-resolved spectroscopy†

Hanchang Huang, ‡[a] Maohui Yuan, ‡[a] Zhongyang Xing, ‡[a] Wenda Cui,[ab] Tongcheng Yu,[ab] Shuai Hu,[a] Guomin Zhao,[ab] Chuan Guo*[ab] and Kai Han *[ac]

Received 18th July 2022,
Accepted 21st September 2022

DOI: 10.1039/d2tc03013f

rsc.li/materials-c

In lanthanide-sensitized upconversion (UC) nanomaterials, the typical sensitizer Yb^{3+} can significantly modulate the codoped activator (such as Er^{3+} ions) to generate multiband transitions. However, the kinetics of these multiband emissions affected by the Yb^{3+} concentration remains unclear. In this work, we employ nanosecond time-resolved spectroscopy to investigate a single optically trapped $NaYF_4$:Yb/Er microcrystal (MC) doped with different Yb^{3+} concentrations. Interestingly, high doping Yb^{3+} ions shorten the UC response time by a factor of 10 (from ~1 μs to ~100 ns) compared to low doping Yb^{3+}. Meanwhile, 430 nm light ($^4G_{7/2} \rightarrow {}^4I_{11/2}$) emitted before 654 nm ($^4F_{9/2} \rightarrow {}^4I_{15/2}$) with Yb^{3+} dramatically increasing (opposite to the normal low Yb^{3+} doping cases), representing a new four-photon pathway ($^4I_{15/2} \rightarrow {}^4I_{11/2} \rightarrow {}^4F_{7/2} \rightarrow {}^2H_{11/2} \rightarrow {}^4S_{3/2} \rightarrow {}^2G_{7/2} \rightarrow {}^4G_{11/2} \rightarrow {}^2H_{9/2} \rightarrow {}^2D_{5/2} \rightarrow {}^4G_{7/2}$). Furthermore, we observed a broad range of time-dependent emission color, changing from being initially green over near-white to red. Particularly, the red emission is dominated in the decay process, yielding insight into the fundamental multiband UC kinetics. The result shows that varying the Yb^{3+} doping concentration provides a way to control the energy flow between the energy levels of Er^{3+} ions, which can modulate the response time and color evolution of UC on Yb/Er doped materials. This can direct the prospective development of fast-response optoelectronic devices, photocatalysis, and UC displays in the future.

Introduction

Luminescence modulation of micron-sized materials has a wide range of applications in the field of optics.[1,2] Lanthanide-based upconversion (UC) materials have the unique ability to convert two or more near-infrared photons to a higher energy photon,[3] thus have been increasingly used in photocatalysis,[4,5] photovoltaics,[6] photodynamic therapy,[7] and anticounterfeiting.[8] One of the most studied UC converters is β-$NaYF_4$:Yb/Er, mainly because of the low phonon energy of the host,[9] large absorption cross-section of sensitizers (Yb^{3+}) at near-infrared excitation (around 976 nm),[10,11] and abundant energy levels of activators (Er^{3+}).[12,13] To improve the UC efficiency of β-$NaYF_4$:Yb/Er, several strategies have been applied,[14] such as changing substrates,[15] using core–shell structures,[16] and modifying the surface of particles.[17] But all these works were based on a Yb/Er doping concentration at around 20/2 mol%,[9,18] meaning that almost 80 mol% RE^{3+} contents (such as Y^{3+}) remain optically inactive. Hence, there is still plenty of room to improve the UCL efficiency by further increasing the Yb^{3+} concentration, because a large number of sensitizers (Yb^{3+}) can ensure more photons to be absorbed (by Er^{3+}) in the system. However, when the Yb^{3+} doping concentration increases to a certain level, the UCL would decline or even quench due to the undesired competing processes such as back-energy transfer (BET) and nonradiative decay.[19–22] For example, Li *et al.* demonstrated that the restriction for the doping ratio of Yb^{3+} is the Yb^{3+}–Yb^{3+} energy migration resulting in surface quenching.[22] However, the energy transfer between dense Yb^{3+} and relatively thin Er^{3+} has still not been explained yet. Therefore, investigating the kinetics of highly doped Yb^{3+} in the β-$NaYF_4$:Yb/Er system can help us understand the UC mechanism and design UC crystal structures with higher UCL efficiency.

To study the optical properties of high dopant concentration UC crystals, high excitation irradiance is required to overcome

[a] College of Advanced Interdisciplinary Studies, National University of Defense Technology, Changsha, 410073, China. E-mail: guochuan20@nudt.edu.cn, hankai0071@nudt.edu.cn
[b] Hunan Provincial Key Laboratory of High Energy Laser Technology, Changsha, 410073, China
[c] State Key Laboratory of Pulsed Power Laser Technology, Changsha, 410073, China

† Electronic supplementary information (ESI) available. See DOI: https://doi.org/10.1039/d2tc03013f

‡ These authors contributed equally to this work and should be considered co-first authors.

the decline or even quenching of UCL.[23] Normally, when the near-infrared excitation power is not high enough, the β-$NaYF_4$:Yb/Er materials mainly show green (545/525 nm) and red (650 nm) UC emissions, and sometimes relatively weak blue (410 nm) emission.[9,18] But under high-irradiance excitation, the UCL is significantly enhanced and the multiband UC emission is effectively achieved as the silent energy levels of Er^{3+} are activated.[24] To better understand the kinetics of β-$NaYF_4$:Yb/Er systems with different Yb^{3+} doping concentrations (especially highly doped), high-power excitation laser is needed to enable multiband UC emissions. Previously, we had developed a sophisticated experimental setup called optical trapping time-resolved photoluminescence spectroscopy (OT-TRPLS), which combines a 1342 nm optical tweezer[25,26] and an advanced time-resolved photoluminescence device with a 976 nm excitation nanosecond-pulsed (ns-pulsed) laser.[27] This allows for measuring the transient spectra at a nanosecond timescale while trapping a single MC to avoid the anisotropy from the movement of the measured MC itself[28–30] and interactions from the surrounding MCs.[31]

In this work, we systematically investigate the impact of Yb^{3+} concentration on multiband emissions in a single optically trapped $NaYF_4$:Yb/Er MC through the OT-TRPLS platform. The kinetics of multiband emissions was determined based on the time-resolved spectra and the multiband color variation dependent on the decay time (from being green over near-white to red) was also quantitatively demonstrated. Interestingly, highly doped Yb^{3+} MC (over 40 mol%) populated the characteristic $^4G_{7/2}$ energy level of Er^{3+} (the highest energy level that a four-photon absorption can achieve) as fast as ~0.1 μs after excitation, whereas a timescale of ~1 μs is obtained for the lowly doped Yb^{3+} MC (lower than 20 mol%). Besides, high doping Yb^{3+} concentration can generate a new populating pathway ($^4I_{15/2} \rightarrow {}^4I_{11/2} \rightarrow {}^4F_{7/2} \rightarrow {}^2H_{11/2} \rightarrow {}^4S_{3/2} \rightarrow {}^2G_{7/2} \rightarrow {}^4G_{11/2} \rightarrow {}^2H_{9/2} \rightarrow {}^2D_{5/2} \rightarrow {}^4G_{7/2}$) to achieve the four-photon UCL. By comparing highly doped Yb^{3+} systems with their low-Yb^{3+} doping counterpart, we find that massive Yb^{3+} ions can accelerate the four-photon population of high energy-level UC (populating $^4G_{7/2}$). Meanwhile, we observed significant red-light emission (dropping from $^4F_{9/2}$ to $^4I_{15/2}$) in the decay process in highly Yb^{3+} doped systems and therefore prove that Yb^{3+} ions can trigger the BET process, making more electrons flow into $^4F_{9/2}$.

Experimental

Materials

Ytterbium(III) chloride ($YbCl_3 \cdot 6H_2O$, 99.99%), erbium(III) chloride ($ErCl_3 \cdot 6H_2O$, 99.99%), and yttrium(III) chloride ($YCl_3 \cdot 6H_2O$, 99.99%) were purchased from Aladdin Industrial Corporation. Sodium fluoride (NaF) and Na_2-ethylenedia-metracetic acid (EDTA-2Na) were supplied by Sinopharm Chemical Reagent Co., Ltd.

Synthesis of β-NaY(Yb)F_4:Yb^{3+}/Er^{3+} MCs

β-NaY(Yb)F_4:Yb^{3+}/Er^{3+} MCs were prepared by the hydrothermal method. According to the doping ratio, $YbCl_3 \cdot 6H_2O$, $ErCl_3 \cdot 6H_2O$, and $YCl_3 \cdot 6H_2O$ were dissolved in 22 mL of deionized water such that the total rare-earth-ion content was 1 mmol, and was stirred ultrasonically until the solution became transparent. 1 mmol EDTA-2Na was added to the mixed solution and stirred thoroughly for 30 minutes. Then 10 mmol NaF was added and stirred for 30 minutes until the solution resembled a jelly appearance. The mixtures above were annealed at 160 °C for 24 hours in a hydrothermal reactor and then cooled down to room temperature. The final products were washed three times with ethanol and deionized water sequentially.

Sample characterization

The monocrystalline β-NaY(Yb)F_4:Yb^{3+}/Er^{3+} MCs are characterized by scanning electron microscopy (SEM). The result (see Fig. 1a–d) shows that the size of MCs slightly increases along with Yb doping concentration, but the overall crystals are about 7 μm in length as hexagonal prisms. The X-ray diffraction (XRD) patterns of the microcrystals were recorded using an X-ray diffractometer with Cu K radiation at 40 kV and 200 mA (Rigaku). The XRD data in the 2θ range from 10° to 70° were collected in the scanning mode at a scanning rate of 10° min^{-1}. The results (see Fig. 1e) demonstrated that the prepared NaY(Yb)F_4 MCs are β-phase crystalline according to the data of the Joint Committee on Powder Diffraction Standards (JCPDS).

Photoluminescence measurements

The time evolution spectra were recorded using the OT-TRPLS setup shown in Fig. 1f, which is equipped with a 976 nm ns-pulsed excitation source and a 1342 nm continuous-wave (CW) optical tweezer. Here the optical tweezer is used to keep the sample MC stable and isolated to avoid unfavorable interactions with the surrounding MCs. Particularly, the 1342 nm laser is chosen because both the Er^{3+} and Yb^{3+} ions have relatively low absorption coefficients at this wavelength.[13,32] A color-complementary metal oxide semiconductor (CMOS) camera is used to monitor the *in situ* optical trapping process as shown in Fig. 1g–j. The excitation power density is ~0.32 GW cm^{-2} with a 15 ns pulse width. A spectrometer equipped with an image intensified charge-coupled device (ICCD) camera is utilized to detect the time evolution spectra with the synchronous triggering of a 976 nm ns-pulsed laser at a repetition rate of 37 Hz. The power efficiency is shown in Fig. S1 and S2 (ESI†). Using the HAMAMATSU system C9920-02G, the quantum efficiencies of the prepared β-NaY(Yb)F_4:Yb^{3+}/Er^{3+} MCs (Yb 10/40/90 mol%) in aqueous solutions are found to be 0.04%, 0.016%, and 0.01%, respectively.

Results and discussion

We obtained the time evolution spectra (Fig. 2a and b) of a single optically trapped $NaYF_4$:Yb/Er (60/2 mol%) MC after the excitation of the 976 nm ns-pulsed laser and observed the rise and decay process of multiband UCL of Er^{3+} ions. The results show that the multiband UCL process has an obvious sequence

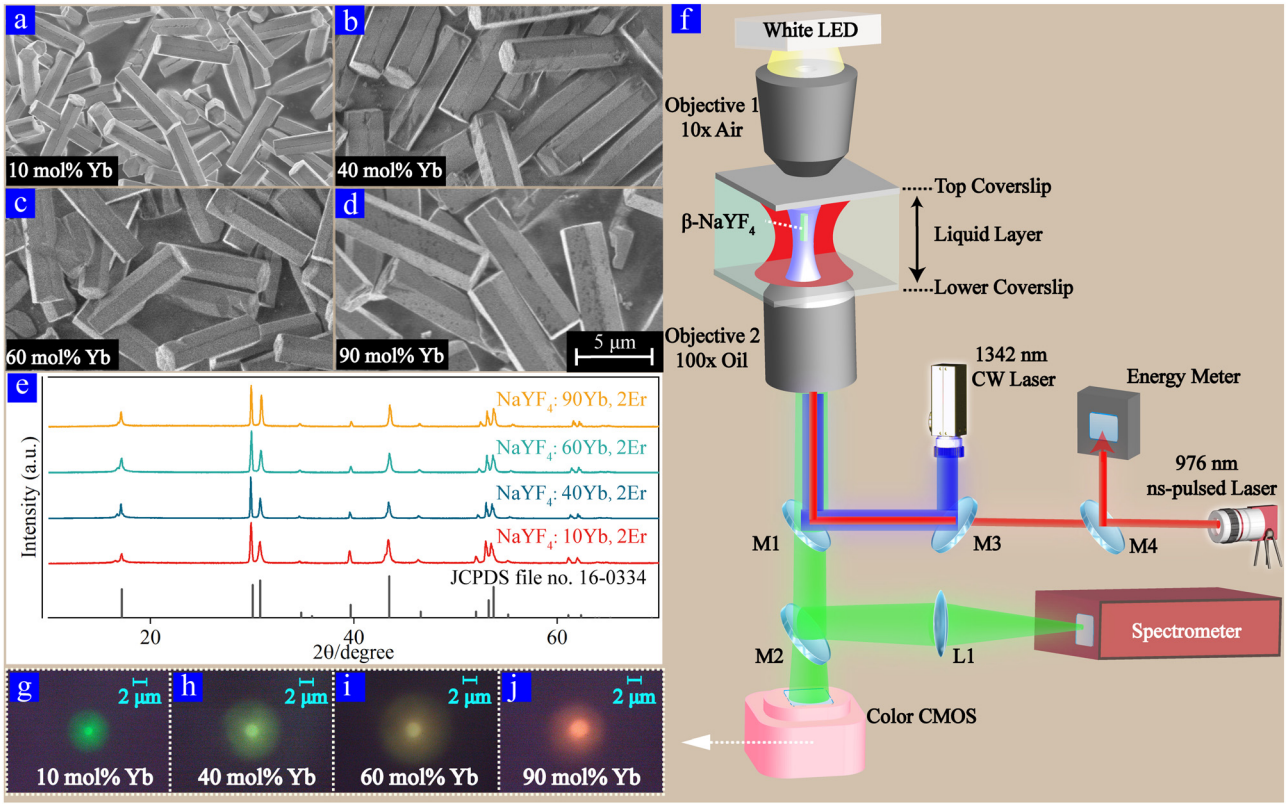

Fig. 1 SEM micrographs of (a–d) β-NaY(Yb)F_4:2% Er/*x*% Yb (*x* = 10, 40, 60, 90) MCs. (e) XRD patterns of the as-prepared β-NaY(Yb)F_4:2% Er/*x*% Yb (*x* = 10, 40, 60, 90) MCs compared to the known peaks of the hexagonal phase of $NaYF_4$. (f) Schematics of the OT-TRPLS setup for multiband UCL detection under laser excitation. The main components are as follows, M1: dichroic mirror for short wave pass, cutoff wavelength is 900 nm; M2: beamsplitter; M3: beam combining mirror for 976 nm laser and 1342 nm laser; M4: beamsplitter; 1342 CW laser and 976 ns-pulsed laser were coaxial before reaching the objective lens. (g–j) Real-time monitoring of the captured single β-NaY(Yb)F_4:2% Er/*x*%Yb (*x* = 10, 40, 60, and 90) MCs by a CMOS camera under 976 nm ns-pulsed laser excitation at the integration time of 50 ms.

of rising and decay at different wavelengths. Furthermore, based on the time evolution spectra, the CIE chromaticity coordinates are calculated and shown in Fig. 2c, which reveals the evolutionary color of the single $NaYF_4$:Yb/Er (60/2 mol%) MC after 976 nm ns-pulsed excitation. The color of a single $NaYF_4$:Yb/Er (60%/2%) MC changed from initially green over near-white to red, which demonstrates that we achieved the near-white color in a single $NaYF_4$:Yb/Er doped with high Yb^{3+} concentration. The color evolution originates from the difference in the rise and decay of the UCL at different wavelengths, which requires analyzing populating processes of energy levels corresponding to these emissions. We subsequently focused on the main UCL peaks, which can be clearly distinguished from each other. According to the previous studies,[12,24,33–37] transient spectra of multiband UCL are determined based on the emission wavelengths and their corresponding transitions, as shown in Fig. 2d.

To further investigate the UC kinetics of single $NaYF_4$:Yb/Er (60%/2%) MC after excitation, we plot a diagram of the populating processes of Yb^{3+} and Er^{3+} ions based on the time evolution spectra. Fig. 3a presents the populating and multiband UCL emitting processes, as well as the decay times of different UC emissions (Fig. 3b). There are two main populating pathways in the Yb–Er systems, *i.e.*, pathway A ($^4I_{15/2} \rightarrow {}^4I_{11/2} \rightarrow {}^4F_{7/2} \rightarrow {}^2H_{11/2} \rightarrow {}^4S_{3/2} \rightarrow {}^2G_{7/2} \rightarrow {}^4G_{11/2} \rightarrow {}^2H_{9/2} \rightarrow {}^4F_{5/2} \rightarrow {}^2K_{13/2}$) and pathway B ($^4I_{15/2} \rightarrow {}^4I_{11/2} \rightarrow {}^4I_{13/2} \rightarrow {}^4F_{9/2} \rightarrow {}^2H_{9/2} \rightarrow {}^2D_{5/2}$).[24,33,38,39] The UCL at 542 nm ($^4S_{3/2} \rightarrow {}^4I_{15/2}$), 522 nm ($^2H_{11/2} \rightarrow {}^4I_{15/2}$), 496 nm ($^4F_{7/2} \rightarrow {}^4I_{15/2}$), 505 nm ($^4G_{11/2} \rightarrow {}^4I_{13/2}$), and 384 nm ($^4G_{11/2} \rightarrow {}^4I_{15/2}$) emits within 50 ns after excitation, which originated from the efficient populating channel of $^4I_{15/2} \rightarrow {}^4I_{11/2} \rightarrow {}^4F_{7/2} \rightarrow {}^2H_{11/2} \rightarrow {}^4S_{3/2} \rightarrow {}^2G_{7/2} \rightarrow {}^4G_{11/2}$ from pathway A and the processes of BET-1 ($^4S_{3/2} \rightarrow {}^4I_{11/2}$) and BET-2 ($^4G_{11/2} \rightarrow {}^4F_{9/2}$) owing to the high doping of Yb^{3+}.[19–22] In the timescale from 50 ns to 80 ns after excitation, the emergence of 402 nm ($^2P_{3/2} \rightarrow {}^4I_{13/2}$) and 767 nm ($^2P_{3/2} \rightarrow {}^4S_{3/2}$) emissions demonstrates the occurrence of the four-photon process. This reveals that the populating channel of $^4F_{5/2} \rightarrow {}^2K_{13/2} \rightarrow {}^2P_{3/2}$ (pathway A) leads to the population of the $^2P_{3/2}$ level. In addition, 482 nm ($^2K_{15/2} \rightarrow {}^4I_{13/2}$), 575 nm ($^2G_{7/2} \rightarrow {}^4I_{11/2}$), 585nm ($^4G_{9/2} \rightarrow {}^4I_{11/2}$), 410nm ($^2H_{9/2} \rightarrow {}^4I_{15/2}$) and 558 nm ($^2H_{9/2} \rightarrow {}^4I_{13/2}$) emissions indicate that the $^2K_{15/2}$, $^2G_{7/2}$, $^4G_{9/2}$ and $^2H_{9/2}$ levels can accumulate electron population processes from pathway A and a nonradiative process (nRP). The radiative transition observed within 80 ns after excitation proves that the whole pathway A (including A-4 processes) has operated. However, the radiative transition on pathway B of the

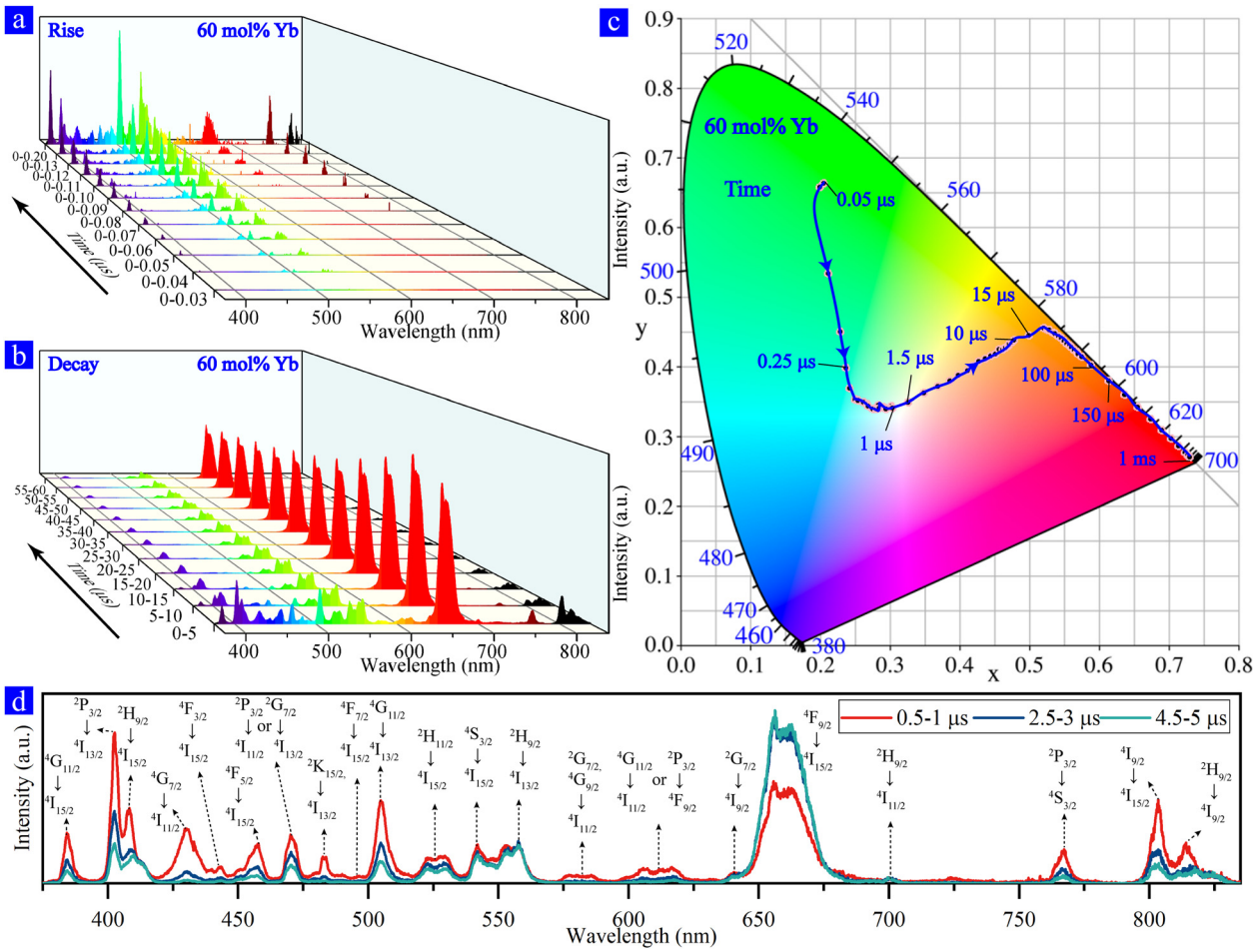

Fig. 2 The 0 moment is the starting point of the 976 nm ns-pulsed excitation. Time evolution spectra of $NaYF_4$:Yb/Er (60/2 mol%) determined using the superimposed transient spectrum at the same moment, 200 times. (a) The temporal evolution of spectra was acquired in a step of 0.01 μs from moment 0. (b) The temporal evolution of spectra was acquired with an integration time of 5 μs. (c) CIE chromaticity coordinates for the multiband UCL of a single β-$NaYF_4$:Yb/Er (60/2 mol%) MC based on time evolution. (d) Transient spectra of the single β-$NaYF_4$:Yb/Er (60%/2%) MC for different time periods with an integration time of 0.5 μs.

two-photon and four-photon processes has not been observed such as 654 nm ($^4F_{9/2} \rightarrow {}^4I_{15/2}$) and 430 nm ($^4G_{7/2} \rightarrow {}^4I_{11/2}$) emissions. Although the $^2H_{9/2}$ energy level can accumulate electron population and produce radiative transition at 410 nm and 558 nm by A-3 and B-3 processes, no radiation transition was observed at 654 nm indicating that the B-3 and B-2 processes are ineffective. This demonstrates that pathway A is more efficient than pathway B in highly-Yb^{3+} doped $NaYF_4$:Yb/Er MCs.

The existence of a new populating process ($^4I_{15/2} \rightarrow {}^4I_{11/2} \rightarrow {}^4F_{7/2} \rightarrow {}^2H_{11/2} \rightarrow {}^4S_{3/2} \rightarrow {}^2G_{7/2} \rightarrow {}^4G_{11/2} \rightarrow {}^2H_{9/2} \rightarrow {}^2D_{5/2} \rightarrow {}^4G_{7/2}$) is suggested according to the observation of 430 nm at 90 ns, which means the B-4 process has operated effectively. However, 654 nm emission was not observed at this time-scale indicating that the B-2 and B-3 processes are not efficient, which implies that pathway A in $NaYF_4$:Yb/Er (60/2 mol%) can provide electrons to prompt the B-4 process. In $NaYF_4$:Yb/Er (60/2 mol%) MCs, pathway A is completed first, then the B-4 process is followed, and finally the B-2 and B-3 processes are performed.

The observation of the 654 nm emission from 90 ns to 110 ns indicates that the B-2 and B-3 processes occur efficiently, which is associated with the $^4I_{13/2}$ level.[40] The electron population accumulation at the $^4I_{13/2}$ level can prompt the B-2 ($^4I_{13/2} \rightarrow {}^4F_{9/2}$) process and 654 nm emission ($^4F_{9/2} \rightarrow {}^4I_{15/2}$), as well as the B-3 ($^4F_{9/2} \rightarrow {}^2H_{9/2}$) process. Compared with pathway A, the reason for the slow operation of pathway B is the slow decay of $^4I_{11/2} \rightarrow {}^4I_{13/2}$ nRP, which was mentioned by Lee *et al.*[41] The 803 nm emission ($^4I_{9/2} \rightarrow {}^4I_{15/2}$), which occurs based on the 654 nm emission from 110 ns to 120 ns, implies that the nRP of $^4F_{9/2} \rightarrow {}^4I_{9/2}$ prompts the radiative transition of $^4I_{9/2}$ energy level.

We have also observed distinct emissions at 456 nm ($^4F_{5/2} \rightarrow {}^4I_{15/2}$), 443 nm ($^4F_{3/2} \rightarrow {}^4I_{15/2}$), 617 nm ($^2P_{3/2} \rightarrow {}^4F_{9/2}$ or $^4G_{11/2} \rightarrow {}^4I_{11/2}$), 640 nm ($^2G_{7/2} \rightarrow {}^4I_{9/2}$), and 817 nm ($^2H_{9/2} \rightarrow {}^4I_{9/2}$) from 90 ns to 200 ns. The UCL at these wavelengths appears relatively late, considering that the energy levels $^4F_{5/2}$, $^4F_{3/2}$, $^2P_{3/2}$, $^4G_{11/2}$, $^2G_{7/2}$, and $^2H_{9/2}$ have already accumulated the electron population before 90 ns as analyzed above. There might be two

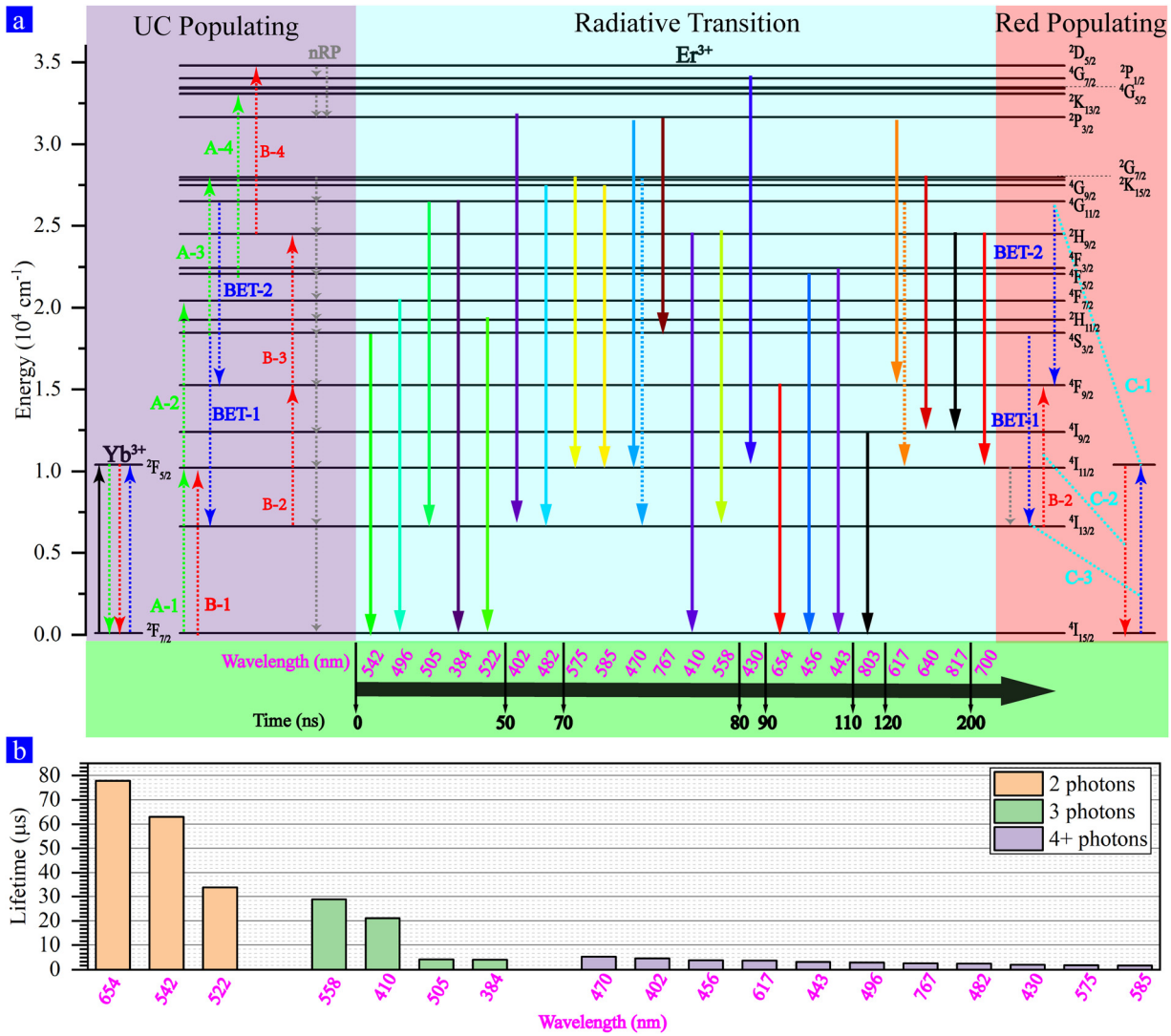

Fig. 3 (a) Schematic representation of the transition kinetics during the first 200 ns after the 976 nm ns-pulsed excitation. The purple part shows the process of establishing electron populations and the nRP. The blue part shows the all radiative transition of multiband UCL. The red part shows the main populating process of red emission enhancement. The green part shows the rise sequence of multiband UCL along with time. (b) The multiband UCL lifetimes of a single β-$NaYF_4$:Yb/Er (60%/2%) MC.

explanations for this; (1) these UC emissions are extremely weak that they cannot be detected before the moment of 90 ns; and (2) only the accumulation of a sufficient number of electron population at the corresponding emitting levels can generate the radiative transitions at these wavelengths.

We have noticed that the UCL at all the wavelengths declined significantly from 0–5 μs to 5–10 μs (except 654 nm), which showed an increasing trend in contrast (see Fig. 2b). The decline happened because the energy that the sensitizer Yb^{3+} can provide to the activator Er^{3+} decreases after excitation, and thus fewer electrons can be populated to the upper energy levels in the activator along with time. The lifetimes of multiband UCLs at different wavelengths are shown in Fig. 3b.[42] In this figure, we divided the wavelengths into three groups according to the number of absorbed photons (two, three, or four), which were determined by the power of the incident laser originally.[33] It shows that the lifetime of UCL decreased as the number of absorbed photons increased in lanthanide-doped systems, suggesting that the UCL lifetime relates not only to the energy level lifetime but also to the energy flow network of the whole UC system.[43] On the other hand, the increase of the 654 nm emission ($^4F_{9/2} \rightarrow {}^4I_{15/2}$) shows that more electrons were populated to $^4F_{9/2}$, which can be caused by the paths relating to the processes of BET-1, BET-2, and B-2 (labeled as C-3, C-1, and C-2, respectively, in Fig. 3a). The first path is the BET-2 process, where the electrons drop from $^4G_{11/2}$ to $^4F_{9/2}$, while the second combines the BET-1 and B-2 processes, through which the electrons were first dropped from the energy level $^4S_{3/2}$ to $^4I_{13/2}$ (BET-1) and then pumped to $^4F_{9/2}$ (B-2). Due to the BET-2 process, the lifetimes of the 505 nm emission and the 384 nm emission (both drops from $^4G_{11/2}$) were much shorter compared to the other three-photon emissions (410 and 558 nm) as the

electrons at $^4G_{11/2}$ reduced (see Fig. 3b). In the two-photo group presented in Fig. 3b, the 542 nm emission ($^4S_{3/2} \rightarrow {}^4I_{15/2}$) and 522 nm emission ($^2H_{11/2} \rightarrow {}^4I_{15/2}$) decayed faster than the 654 nm emission, which might be due to the BET-1 process that reduced the electron population at the energy levels of $^4S_{3/2}$ and $^2H_{11/2}$.

To further investigate the effect of sensitizer Yb^{3+} on the kinetics of multiband UCL, we recorded the time evolution spectra of rising processes for single NaY(Yb)F_4:Yb/Er MC doped with different concentrations of Yb^{3+} sensitizer, as shown in Fig. 4a–c. The spectra show that the multiband UCL appeared at ~1 μs and ~0.1 μs, respectively (schematic representation of the transition kinetics is shown in Fig. S3–S5, ESI†) when the Yb^{3+} doping concentration was low (10 mol%) and high (40, 60 and 90 mol%); and the 10% Yb^{3+} doping mainly presented two-photon UCL at 522 nm and 542 nm within 100 ns. After ns-pulsed excitation, the electrons in Yb^{3+} sensitizer ions were first populated to the energy level $^2F_{5/2}$ and then dropped back to $^2F_{7/2}$. Through this process, energy was transferred from the sensitizer ions to Er^{3+} activator ions, further populating the electrons in Er^{3+} to higher energy levels. Fig. 4d shows the schematics of how energy transfers within the β-NaY(Yb)F_4:Yb/Er lattice for low Yb^{3+} doping and high Yb^{3+} doping. As the Yb^{3+} doping concentration grows, the surrounding Yb^{3+} ions per Er^{3+} became more and the energy migration is enhanced, resulting in the increase of the energy transferred from Yb^{3+} to Er^{3+}. Particularly, for high Yb^{3+}doping cases, the energy of Yb^{3+}can be transferred to the surrounding

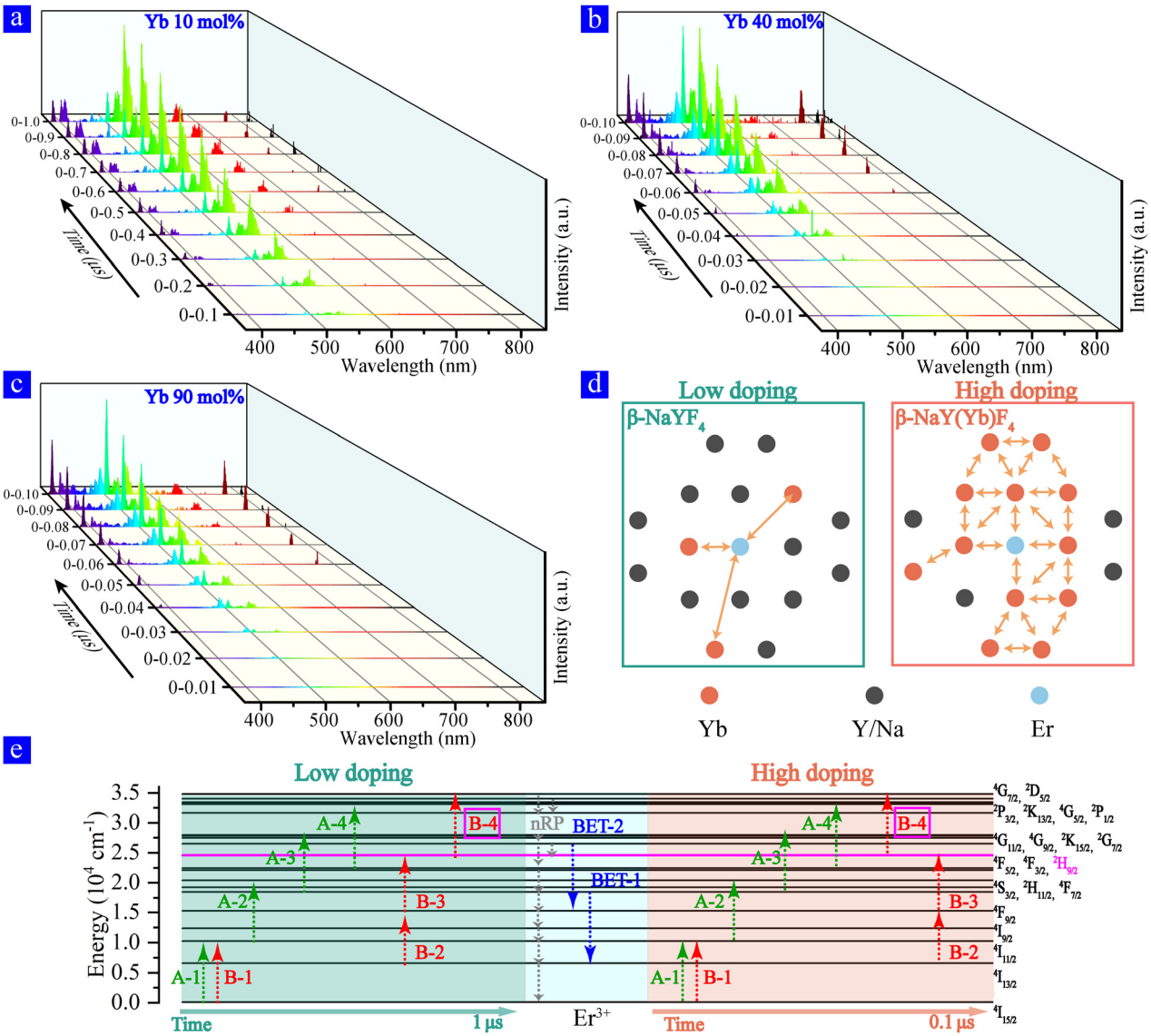

Fig. 4 The 0 moment is the starting point of the 976 nm ns-pulsed excitation. Time evolution spectrum of NaY(Yb)F_4:Yb/Er (*X*/2 mol%) determined using the superimposed transient spectrum at the same moment. *X* = (a) 10, (b) 40, and (c) 90. (d) Schematic representation showing the distributing difference of ions between high-doping and low-doping in a single NaY(Yb)F_4:Yb/Er MC. (e) Schematic representation showing the difference of the populating processes between high-doping and low-doping in a single NaY(Yb)F_4:Yb/Er MC.

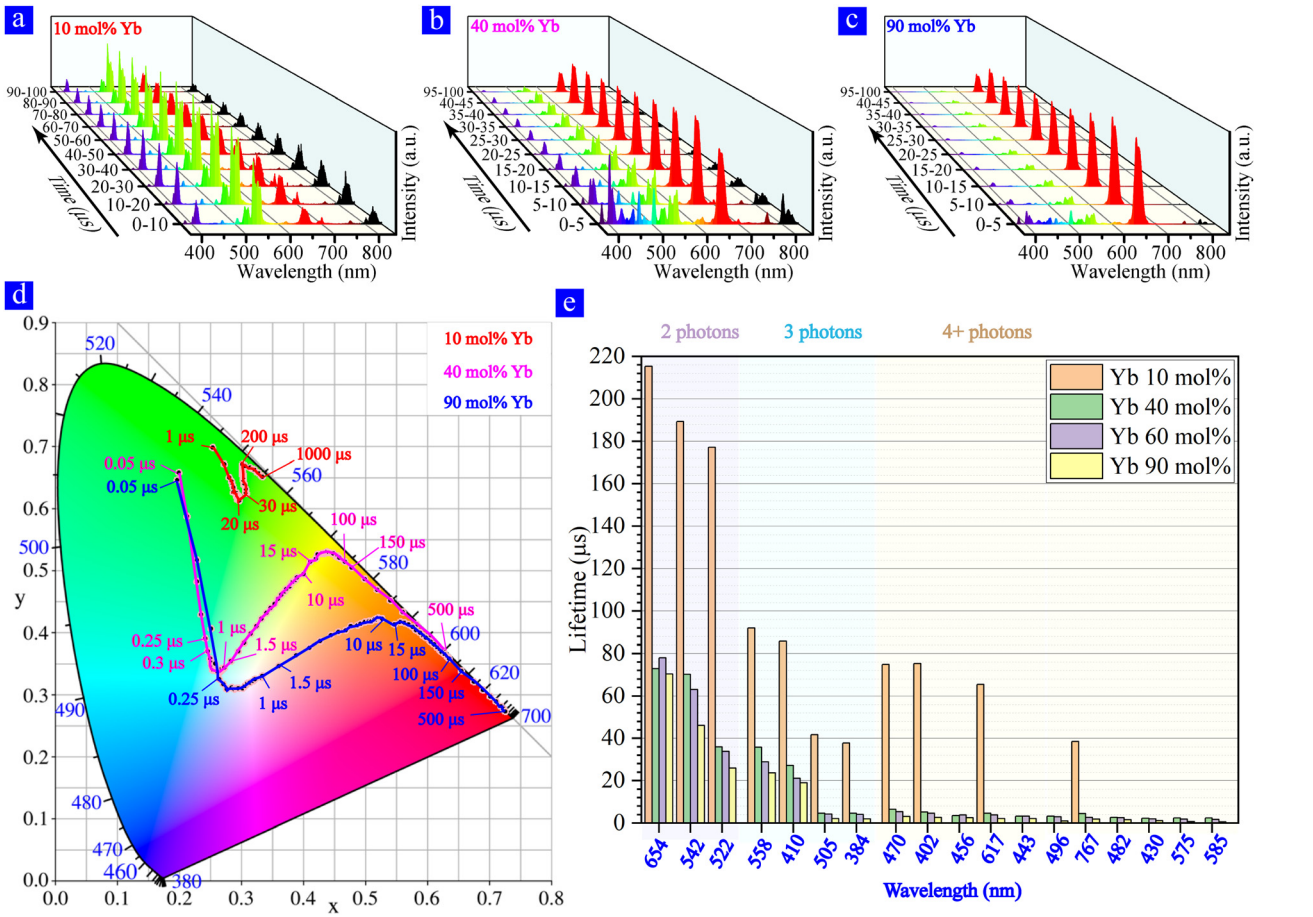

Fig. 5 The 0 moment is the starting point of the 976 nm ns-pulsed excitation. Time evolution spectrum of NaY(Yb)F_4:Yb/Er (*X*/2 mol%) determined using the superimposed transient spectrum at the same moment. *X* = (a) 10, (b) 40, and (c) 90. (d) CIE chromaticity coordinates for the multiband UCL of the single β-NaY(Yb)F_4:Yb/Er MC with different Yb^{3+} concentrations based on the time evolution spectrum. (e) The multiband UCL lifetimes of a single β-NaY(Yb)F_4:Yb/Er MC with different doping concentrations.

Er^{3+} ions as well as the neighboring Yb^{3+} ions.[44–46] Therefore, Er^{3+} ions can acquire more instantaneous energy, and thus the multiband UCL process can be speeded up when the Yb^{3+} doping concentration is high enough.

Apart from the acceleration of the UC process, there are also changes in the populating process between low and high doping (Fig. 4e). Commonly, in Yb/Er systems the populating process operates through pathway A (A-1, A-2, A-3, A-4, and nRP) and pathway B (B-1, B-2, B-3, B-4 and nRP), with B-3 happening after A-4.[27] But when Yb doping concentration is high, B-4 ($^2H_{9/2} \rightarrow {}^2D_{5/2}$) happens superior to B-3 ($^4F_{9/2} \rightarrow {}^2H_{9/2}$) because $^2H_{9/2}$ accumulates abundant electrons due to the enhancement of pathway A-3 and the following nRP. This shows that pathway A can promote the operation of pathway B.

Furthermore, we have investigated the decay processes at different Yb^{3+} doping concentrations (as shown in Fig. 5) and found a strong red emission (at 654 nm) for high doping (Fig. 5b and c). This confirms our previous studies on 60% Yb^{3+} that Yb^{3+} ions can enhance the 654 nm emission through the processes of C-1 C-2 and C-3. As shown in Fig. 5d, for highly Yb^{3+} doped MCs (40 and 90 mol%), the CIE chromaticity diagram shows the almost same color variation trend. For the 90% Yb^{3+} doped MC, the near-white color appeared at around 500 ns and the red color appeared at around 100 μs. However, the low Yb^{3+} doped MC (10 mol%) initially emits green color (dominated by the two-photon UCL), and gradually includes blue-violet color (originated from the three- or four-photon UCL). As the Yb^{3+} concentration increases, the lifetime of multiband UCL decreases as shown in Fig. 5e, possibly owing to the energy loss of Yb^{3+} sensitizers at considerably high concentrations.[43] The phenomena of measuring β-NaY(Yb)F_4: Yb/Er (90/2 mol%) and β-$NaYbF_4$: Er (2 mol%) MCs are similar, and relevant results are detailed in Fig. S6–S9 (ESI†).

Conclusions

In summary, we applied nanosecond time-resolved spectroscopy to an optically trapped single β-NaY(Yb)F_4:Yb/Er MC varying the doping concentration of the Yb^{3+} sensitizer. First, we recorded the time evolution spectra of a β-$NaYF_4$:Yb/Er (60/2 mol%) MC after ns-pulsed high-irradiance excitation,

from which we calculated CIE chromaticity to show color evolution (from initially green over near-white to red). The sequences of UCL rising processes at different wavelengths are determined based on the time evolution spectra, which reveals a new 4-photon populating process ($^4I_{15/2} \rightarrow {}^4I_{11/2} \rightarrow {}^4F_{7/2} \rightarrow {}^2H_{11/2} \rightarrow {}^4S_{3/2} \rightarrow {}^2G_{7/2} \rightarrow {}^4G_{11/2} \rightarrow {}^2H_{9/2} \rightarrow {}^2D_{5/2} \rightarrow {}^4G_{7/2}$). Furthermore, we show the difference in the populating pathway between high and low doping concentrations. We found that the timescale to achieve pathway A and pathway B is one order of magnitude smaller for high doping ($\sim$0.1 μs) compared to low doping ($\sim$1 μs). However, limited by the BET process and the energy decay originating from the Yb^{3+} sensitizer, the multiband UCL lifetime has shortened, and the proportion of red-light emission keeps increasing, as the Yb^{3+} doping concentration increases. The result indicates that a reasonably large number of Yb^{3+} ions can effectively modulate the response speed of the multiband UC process, change photophysical pathways, and control energy flow to the $^4F_{9/2}$ energy level leading to a huge percentage of red emission. Our findings provides a way to understand the impact of Yb^{3+} concentration on UC, which has potential applications in fast-response optoelectronic devices and UC displays in the future.

Author contributions

H. H., M. Y. and K. H. conceived the work. M. Y., Z. X., C. G., K. H. and G. Z. provided guidance and supervision. T. Y., S. H. and W. C. characterized the upconversion microcrystals by SEM and XRD. H. H. and C. G. built the photoluminescence platform. H. H. performed the spectroscopy experiment. H. H., M. Y. and Z. X. analyzed the data and wrote the manuscript. All authors participated in the discussion and finalization of the manuscript.

Conflicts of interest

The authors declare that they have no known competing financial interests or personal relationships that could have appeared to influence the work reported in this paper.

Acknowledgements

This work was supported financially by the Science Fund for Excellent Young Scholars (2017X016), Innovation Fund for Young Scholars (19QNCXJ) and the State Key Laboratory of Laser Interaction with Matter Foundation (SKLLIM1708). We are thankful to Xi'an ruixi Biological Technology Co., Ltd for providing us with the β-$NaYF_4$ microcrystals.

Notes and references

1 Z. Dong, N. Zhang, Y. Wang, J. Wu, Q. Gan and W. Li, *Adv. Funct. Mater.*, 2019, **29**, 1904453.
2 Z. Y. Yang, J. Y. Xu, P. Wang, X. J. Zhuang, A. L. Pan and L. M. Tong, *Nano Lett.*, 2011, **11**, 5085–5089.
3 F. Auzel, *Chem. Rev.*, 2004, **104**, 139–173.
4 S. Liu, J. Huang, L. Yan, N. Song, P. Zhang, J. He and B. Zhou, *J. Mater. Chem. A*, 2021, **9**, 4007.
5 Q. Tian, W. Yao, Z. Wu, J. Liu, J. Liu, W. Wu and C. Jiang, *J. Mater. Chem. A*, 2017, **5**, 23566.
6 F. Xu, Y. Sun, H. Gao, S. Jin, Z. Zhang, H. Zhang, G. Pan, M. Kang, X. Ma and Y. Mao, *ACS Appl. Mater. Interfaces*, 2021, **13**, 2674–2684.
7 X. Wu, P. Yan, Z. Ren, Y. Wang, X. Cai, X. Li, R. Deng and G. Han, *ACS Appl. Mater. Interfaces*, 2019, **11**, 385–393.
8 X. Liu, Y. Wang, X. Li, Z. Yi, R. Deng, L. Liang, X. Xie, D. T. B. Loong, S. Song, D. Fan, A. H. All, H. Zhang, L. Huang and X. Liu, *Nat. Commun.*, 2017, **8**, 899.
9 J. F. Suyver, J. Grimm, M. K. van Veen, D. Biner, K. W. Krämer and H. U. Güdel, *J. Lumin.*, 2006, **117**, 1–12.
10 F. Vetrone, J.-C. Boyer, J. A. Capobianco, A. Speghini and M. Bettinelli, *J. Appl. Phys.*, 2004, **96**, 661–667.
11 B. S. Cao, Y. Y. He, L. Zhang and B. Dong, *J. Lumin.*, 2013, **135**, 128–132.
12 D. G. O'Shea, J. M. Ward, B. J. Shortt, M. Mortier, P. Féron and S. N. Chormaic, *Eur. Phys. J.: Appl. Phys.*, 2007, **40**, 181–188.
13 G. Yao, C. Lin, Q. Meng, P. Stanley May and M. T. Berry, *J. Lumin.*, 2015, **160**, 276–281.
14 S. Han, R. Deng, X. Xie and X. Liu, *Angew. Chem., Int. Ed.*, 2014, **53**, 11702–11715.
15 G. Y. Lee, K. Jung, H. S. Jang, J. Kyhm, I. K. Han, B. Park, H. Ju, S. J. Kwon and H. Ko, *Nanoscale*, 2016, **8**, 2071–2080.
16 F. Vetrone, R. Naccache, V. Mahalingam, C. G. Morgan and J. A. Capobianco, *Adv. Funct. Mater.*, 2009, **19**, 2924–2929.
17 P. Yuan, Y. H. Lee, M. K. Gnanasammandhan, Z. Guan, Y. Zhang and Q. H. Xu, *Nanoscale*, 2012, **4**, 5132–5137.
18 M. Haase and H. Schafer, *Angew. Chem., Int. Ed.*, 2011, **50**, 5808–5829.
19 J. Wang, R. Deng, M. A. MacDonald, B. Chen, J. Yuan, F. Wang, D. Chi, T. S. Hor, P. Zhang, G. Liu, Y. Han and X. Liu, *Nat. Mater.*, 2014, **13**, 157–162.
20 D. Xu, C. Liu, J. Yan, S. Yang and Y. Zhang, *J. Phys. Chem.*, 2015, **119**, 6852–6860.
21 D. Gao, X. Zhang, B. Chong, G. Xiao and D. Tian, *Phys. Chem. Chem. Phys.*, 2017, **19**, 4288–4296.
22 B. Shen, S. Cheng, Y. Gu, D. Ni, Y. Gao, Q. Su, W. Feng and F. Li, *Nanoscale*, 2017, **9**, 1964–1971.
23 J. Zhao, D. Jin, E. P. Schartner, Y. Lu, Y. Liu, A. V. Zvyagin, L. Zhang, J. M. Dawes, P. Xi, J. A. Piper, E. M. Goldys and T. M. Monro, *Nat. Nanotechnol.*, 2013, **8**, 729–734.
24 M. Yuan, R. Wang, C. Zhang, Z. Yang, W. Cui, X. Yang, N. Xiao, H. Wang and X. Xu, *J. Mater. Chem. C*, 2018, **6**, 10226–10232.
25 I. D. Stoev, A. Caciagli, Z. Xing and E. Eiser, *Conference on Optical Trapping and Optical Micromanipulation XV*, San Diego, CA, 2018, vol. 10723, DOI: **10.1117/12.2318019**.
26 R. W. Bowman and M. J. Padgett, *Rep. Prog. Phys.*, 2013, **76**, 026401.
27 H. Huang, M. Yuan, S. Hu, Y. Zhong, W. Cui, C. Guo, C. Song, G. Zhao and K. Han, *J. Mater. Chem. C*, 2022, **10**, 9208–9215.

28 P. Rodriguez-Sevilla, Y. Zhang, N. de Sousa, M. I. Marques, F. Sanz-Rodriguez, D. Jaque, X. Liu and P. Haro-Gonzalez, *Nano Lett.*, 2016, **16**, 8005–8014.
29 P. Rodriguez-Sevilla, L. Labrador-Paez, D. Wawrzynczyk, M. Nyk, M. Samoc, A. K. Kar, M. D. Mackenzie, L. Paterson, D. Jaque and P. Haro-Gonzalez, *Nanoscale*, 2016, **8**, 300–308.
30 J. Kim, R. Chacon, Z. Wang, E. Larquet, K. Lahlil, A. Leray, G. Colas-des-Francs, J. Kim and T. Gacoin, *Nat. Commun.*, 2021, **12**, 1943.
31 P. Rodriguez-Sevilla, H. Rodriguez-Rodriguez, M. Pedroni, A. Speghini, M. Bettinelli, J. G. Sole, D. Jaque and P. Haro-Gonzalez, *Nano Lett.*, 2015, **15**, 5068–5074.
32 C. Renero-Lecuna, R. Martín-Rodríguez and R. Valiente, *Chem. Mater.*, 2011, **23**, 3442–3448.
33 F. Frenzel, C. Würth, O. Dukhno, F. Przybilla, L. M. Wiesholler, V. Muhr, T. Hirsch, Y. Mély and U. Resch-Genger, *Nano Res.*, 2021, **14**, 4107–4115.
34 Z. X. Cheng, S. J. Zhang, F. Song, H. C. Guo, J. R. Han and H. C. Chen, *J. Phys. Chem. Solids*, 2002, **63**, 2011–2017.
35 D. K. Sardar, J. B. Gruber, B. Zandi, J. A. Hutchinson and C. W. Trussell, *J. Appl. Phys.*, 2003, **93**, 2041–2046.
36 X. Y. Chen, E. Ma and G. K. Liu, *J. Phys. Chem. C*, 2007, **111**, 10404–10411.
37 R. T. Wegh, E. V. D. Van Loef, G. W. Burdick and A. Meijerink, *Mol. Phys.*, 2003, **101**, 1047–1056.
38 T. Jung, H. L. Jo, S. H. Nam, B. Yoo, Y. Cho, J. Kim, H. M. Kim, T. Hyeon, Y. D. Suh, H. Lee and K. T. Lee, *Phys. Chem. Chem. Phys.*, 2015, **17**, 13201–13205.
39 R. B. Anderson, S. J. Smith, P. S. May and M. T. Berry, *J. Phys. Chem. Lett.*, 2014, **5**, 36–42.
40 K. Shin, T. Jung, E. Lee, G. Lee, Y. Goh, J. Heo, M. Jung, E. J. Jo, H. Lee, M. G. Kim and K. T. Lee, *Phys. Chem. Chem. Phys.*, 2017, **19**, 9739–9744.
41 E. Lee, M. Jung, Y. Han, G. Lee, K. Shin, H. Lee and K. T. Lee, *J. Phys. Chem. C*, 2017, **121**, 21073–21079.
42 M. Inokuti and F. Hirayama, *J. Chem. Phys.*, 1965, **43**, 1978.
43 A. Teitelboim, B. Tian, D. J. Garfield, A. Fernandez-Bravo, A. C. Gotlin, P. J. Schuck, B. E. Cohen and E. M. Chan, *J. Phys. Chem. C*, 2019, **123**, 2678–2689.
44 Y. Liang, Z. Zhu, S. Qiao, X. Guo, R. Pu, H. Tang, H. Liu, H. Dong, T. Peng, L. D. Sun, J. Widengren and Q. Zhan, *Nat. Nanotechnol.*, 2022, **17**, 524–530.
45 B. Zhou, L. Yan, J. Huang, X. Liu, L. Tao and Q. Zhang, *Nat. Photonics*, 2020, **14**, 760–766.
46 J. Zuo, D. Sun, L. Tu, Y. Wu, Y. Cao, B. Xue, Y. Zhang, Y. Chang, X. Liu, X. Kong, W. J. Buma, E. J. Meijer and H. Zhang, *Angew. Chem., Int. Ed.*, 2018, **57**, 3054–3058.